Science Advances

AAAS

Supplementary Materials for

Full-field imaging of thermal and acoustic dynamics in an individual nanostructure using tabletop high harmonic beams

Robert M. Karl Jr.*, Giulia F. Mancini*, Joshua L. Knobloch, Travis D. Frazer, Jorge N. Hernandez-Charpak, Begoña Abad, Dennis F. Gardner, Elisabeth R. Shanblatt, Michael Tanksalvala, Christina L. Porter, Charles S. Bevis, Daniel E. Adams, Henry C. Kapteyn, Margaret M. Murnane

*Corresponding author. Email: robert.karl@colorado.edu (R.M.K.); giulia.mancini@colorado.edu (G.F.M.)

The PDF file includes:

Other Supplementary Material for this manuscript includes the following:

(available at advances.sciencemag.org/cgi/content/full/4/10/eaau4295/DC1)

Histogram analysis

Figures S2 A-D show the masks made from the two primary peaks (fig. S2 B, C) and the mask from the remaining pixels, showing the second, excluded nanostructure (fig. S2D). Each mask is created by testing each pixel of the image to see if its complex reflectivity lies within the peak, and if so assigning that pixel to the corresponding mask. We determined that neither of the primary masks contains the circular nanostructure, allowing us to systematically exclude it from all subsequent analysis.

We also remark that if the histogram was projected into only amplitude or phase, the peaks would cease to be well-separated. This is due to the different peaks having a finite extent, which causes the two peaks to overlap in the projection, despite being well separated in the complex plane. An example of this is displayed in fig. S2 E, showing the two-dimensional histogram projected onto only amplitude.

Diffraction efficiency

For each time delay, the diffraction efficiency into the first order was calculated by taking the difference in the total intensity in the first order diffraction peak and the total intensity in the unscattered, central diffraction peak. This value was normalized to the total intensity in all three of these peaks (the undiffracted peak and the two, symmetric first order peaks). The diffraction efficiency from the data without the pump beam was subtracted from the data with the pump beam, yielding a differential measurement of the diffraction efficiency.

Image reconstructions

The diffraction patterns from the ptychographic scans were processed by centering the diffraction relative to the maximum value of the average diffraction pattern. A constant background was removed from the images to suppress the noise. The effects of conical diffraction were corrected for using tilted plane correction techniques (*34*). The data were cropped to a size of 512x512 pixels, resulting in a theoretical Abbe resolution of 76nm. The relation between theoretical and realized transverse resolution for this microscope has been explored elsewhere (*35*).

In order to quantify the axial precision, we calculated the height difference between the pump on and pump off reconstructed images for all times before the infrared pulse. The standard deviation of this differential value was calculated for various regions throughout the image. The largest variance observed was 0.009 radians, corresponding to 0.04nm, thus we make a conservative estimate of the precision of this measurement to be 0.5Å.

The complex image of the nickel tapered nanoantenna and the EUV probe were reconstructed using 10550 iterations of the ePIE algorithm (*24*) with Modulus Enforced Probe (*14*) with an object relaxation factor of 1 and a probe relaxation factor of 5. The scan positions were refined using 400 iterations of a position correction algorithm (*36*).

A representative reconstruction of the sample is shown in Fig. 1 (main text); reconstructions of the probe used to measure the tapered and the uniform nanoantenna are shown in figs. S3 (A, B), respectively.

The 2D+1 height maps reported in Fig. 2 (main text) were created from the reconstructed images. First, we used histogram segmentation to separate the tapered nanoantenna and the substrate regions. Following this step, the literature values for the index of refraction for nickel and silicon were used to remove the effect of the Fresnel reflectivity for these two regions (*12*). The phase in the Fresnel-corrected image was unwrapped using a 2D Goldstein branch cut phase unwrapping algorithm (*37*, *38*). After this step, the remaining phase was all attributed to path length differences due to the topography of the sample and converted into height.

The differential height maps displayed in Fig. 2 (main text) are the difference in height between the dataset taken with the laser-driven excitation and without the excitation. The dynamics in the ptychographic images were characterized by considering two different cross-sections of the nanoantenna: one with 1.5μm width, and the other with 2.2μm width, corresponding with the simulated cross-sections (below). At each cross-section, the average height of a 1.1μm region of the substrate located 2.7μm from the edge of the nanoantenna was subtracted from the average height of the center 450nm of the nanoantenna. This difference for the data without the laser-driven excitation was subtracted from the difference with the excitation, giving us a differential measurement of the relative height. The differential height as a function of time, retrieved experimentally, is compared to the same quantity, calculated in the same way, from the two simulated cross-sections (fig. S4). We observe that the simulations and experiment qualitatively agree, showing oscillations with similar amplitude and frequency. Furthermore, the dynamics between the two separate cross-sections of the reconstruction show a different behavior, indicating that the dynamics indeed vary spatially, as observed in the reconstructed image of Fig. 2I and discussed in the main text.

Dynamics simulation

To capture both the thermal transport and acoustic wave physics induced by a laser pulse, we numerically simulate the initial heat-driven displacement and its time evolution (*29*). We performed this simulation on a two-dimensional nanoline cross-section of the nickel tapered nanoantenna to approximate the dynamics at two different locations along its length. In both cross-section simulations, we used a height of 20.5nm for the nickel tapered nanoantenna.

We specifically chose our finite sized substrate to be large enough such that any reflected acoustic waves from the artificial simulation boundaries would not reach the nanostructure within the duration of the simulation. Nonetheless, low-reflecting boundary conditions were in place at the bottom and sides of the substrate to suppress any possible wave reflection. Additionally, the substrate sides and bottom boundaries were implemented as thermally insulating while the exposed surfaces of the substrate and nanostructure were free and insulating. The interface between the nanostructure and substrate has a thermal boundary resistivity of 5nK*m/W to account for possible native oxide layer, interface roughness, or quasi-ballistic transport effects (*1*, *2*). Note that the large nanostructure does not have enough time to dissipate heat in the ≈600ps experimental time window; therefore, the boundary conditions and material

properties specific to the thermal transport (e.g. heat capacity and thermal boundary resistivity) have little effect on the simulation results over this time range. The material properties used in the simulation are seen in Table 1.

For our simulations, we used a similar model as in Nardi *et al.* (*39*). However, we used an approximation that the phonon temperature in the nanostructure starts initially at a higher temperature (600K for 1.5um and 450K for 2.2um). Since the initial strain of the nanostructure corresponds to room temperature, the instantaneous temperature rise causes the impulsive thermal expansion we observe in the experiment. Small time-scale simulations were run incorporating the sub-picosecond electronic excitation of the metallic nanostructure (*40*) which demonstrated that the electron and phonon temperatures thermalize in a few picoseconds and related laser fluences to initial phonon temperatures. Additional simulations were used to show that different initial temperatures just re-scale the surface deformation. Therefore, simple overall scaling of the simulation results can be used to match the pump fluence in the experiment.

The Rayleigh velocities in these materials can be approximately calculated (*31*). Using this approximation, we calculate the Rayleigh velocity of bulk Si to be 4300-5300m/s, and of bulk Ni to be ~2800m/s. However, the Rayleigh velocity of thin film Ni could be up to 10% lower than that of bulk, due to reduced Young's modulus, making the velocity ~2500m/s (*33, 41*).

Dispersion analysis

To test the extraction of acoustic velocities by measuring dispersion relations, a 20nm tall nickel grating with 500nm thick lines with a 2μm period was used as a reference object (fig. S5 C). The behavior of such system has been previously characterized and reported (*42*). The diffraction efficiency into the each diffraction order was analyzed as in the main text to measure the dispersion relation of the acoustic waves. Over the range probed by this experiment, the dispersion relation is linear, with the proportionality constant of 5230±650m/s, indicating that the pseudo-surface acoustic waves (*43*) have velocity similar to that of a SAW in silicon (fig. S5 D).
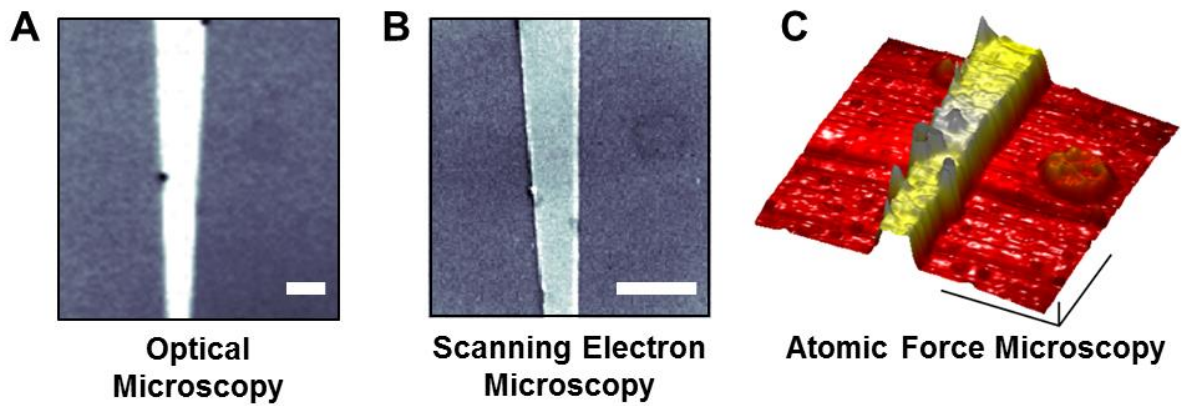
Fig. S1. Preliminary sample characterization. (A) Optical microscope, (B) SEM, and (C) AFM images of the sample. The scale bar to (A) and (B) is 5μm. In (C), the scale bar is 5μmx5μmx15nm.
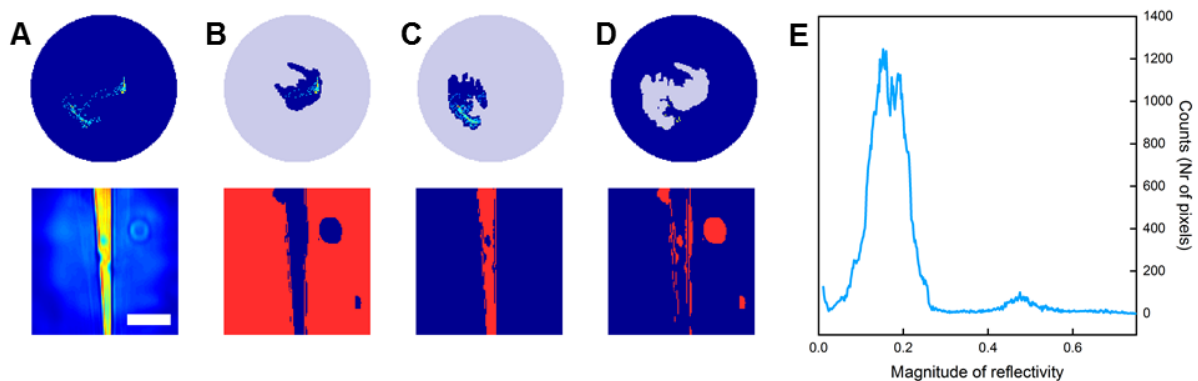

Fig. S2. Histogram analysis. (A to D) Top: two dimensional histogram with different regions highlighted corresponding to the regions shown in the bottom row. Bottom: masked images of the tapered nanoantenna corresponding to the different peaks in the complex histogram. The scale bar is 5μm. (E) Projection of the two dimensional histogram into a one dimensional histogram, showing reduced separation in the two peaks.
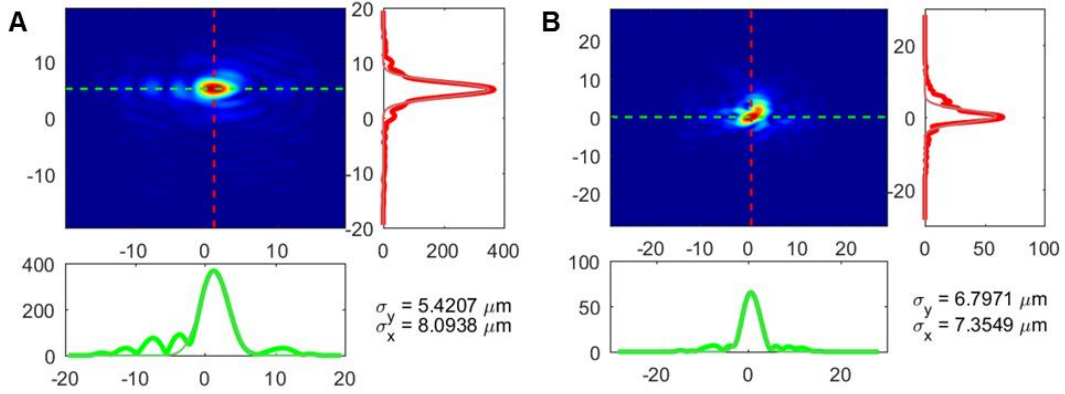
Fig. S3. Reconstructed EUV beam. (A) for the tapered and (B) for the uniform nanoantenna. The sigma values reported are the full width at half maximum for the vertical and horizontal directions.
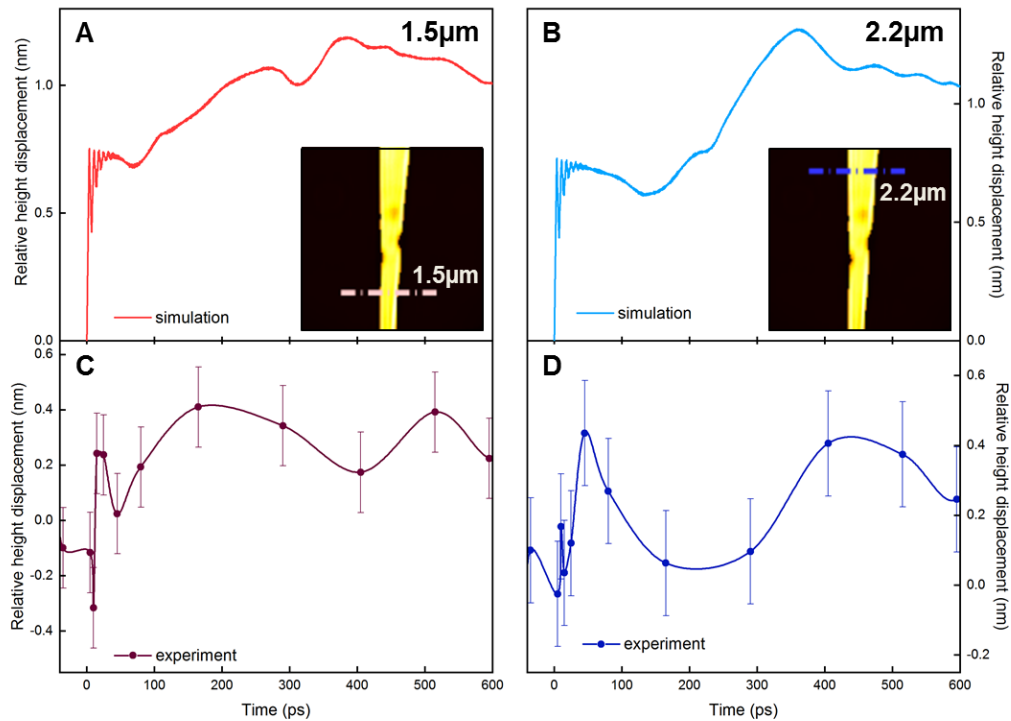
Fig. S4. Comparison of the spatially resolved acoustic dynamics. (A and B) Difference in the height of the tapered nanoantenna and the substrate in the 1.5μm and 2.2μm cross-section simulations, respectively. The insets show the location of these lineouts on the nanoantenna. (C and D) Difference in the height of the tapered nanoantenna and the substrate from lineouts of the experimental reconstructions at the appropriate thicknesses. We remark that the spline lines connecting the data points are a guide to the eye. Errorbars are derived from the variance in the data taken before the pump pulse.
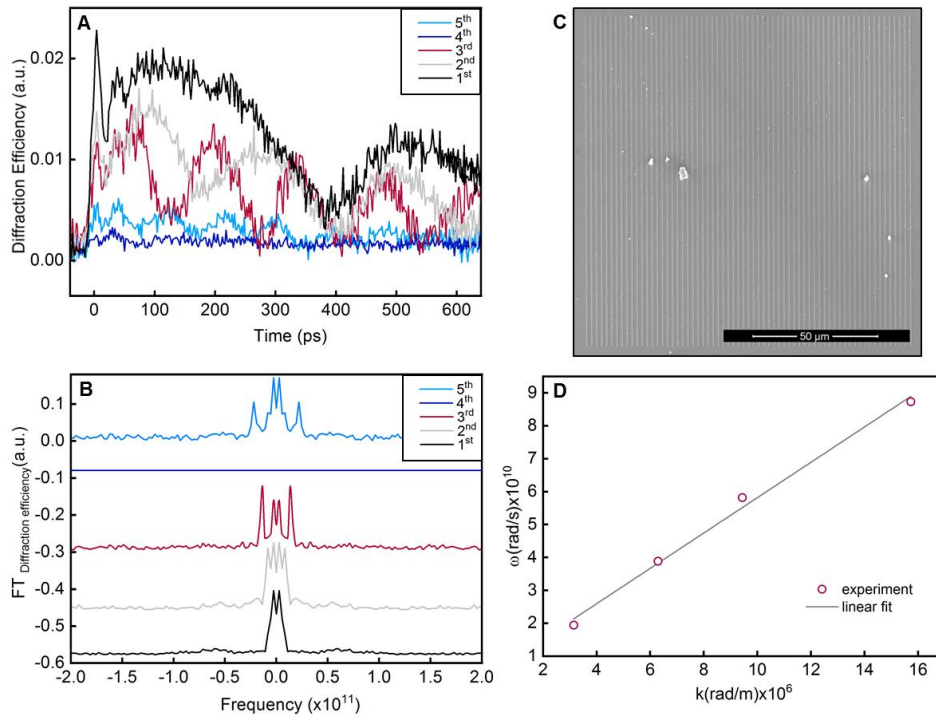
Fig. S5. Analysis of dispersion in a nickel grating on silicon substrate. (A) Transient diffraction efficiency for the first five diffracted orders. (B) Fourier transform of the transient diffraction efficiency for each order. (C) SEM image of the nickel grating sample. (D) Dispersion relation extracted from the diffraction efficiencies with a best fit line.

Table S1. Parameters for material properties used in the simulation. The numbers in parenthesis are references to literature.

Materials	Nickel (Ni)	Silicon (Si)
k [W/(m K)]	90.9 (*44*)	149 (*44*)
ρ [kg/m^3]	8900 (*44*)	2330 (*44*)
α [10^{-6} K^{-1}]	12.77(*45*)	3 (*46*)
C_p [J/(kg K)]	456* (*44*)	710 (*47*)
E [GPa]	219 (*39*)	-
v	0.31 (*39*)	-
C_{11} [GPa]	-	166 (*48*)
C_{12} [GPa]	-	64 (*48*)
C_{44} [GPa]	-	80 (*48*)

412.5 was used for 2.2 µm width simulation

Movie S1. Movie of the 2D+1 height maps form the phase reconstructions displayed as a function of time.

Movie S2. Movie of the complex histograms for each reconstruction. The rotation of one peak relative to the other indicates a change in the height of the nanostructure.

Movie S3. Movies 1 and 2 displayed concurrently, allowing the relation between the images and the histograms to be visualized.